NUCL SCI TECH (2018) 29:117
https://doi.org/10.1007/s41365-018-0449-2

Position-sensitive plastic scintillator detector with WLS-fiber readout

Jia-Ning Dong[1,3] · **Yun-Long Zhang**[1,2] · **Zhi-Yong Zhang**[1,2] · **Dong Liu**[1,2] · **Zi-Zong Xu**[1,2] · **Xiao-Lian Wang**[1,2] · **Shu-Bin Liu**[1,2]

Received: 19 August 2016 / Revised: 18 August 2017 / Accepted: 15 November 2017 / Published online: 4 July 2018

Abstract In this paper, the design, construction, simulation, and performance of a position-sensitive plastic scintillator detector are presented. The readout of the detector uses wavelength-shifting fibers coupled with multi-anode photomultipliers (PMTs) for the *x*- and *y*-dimensions. After calibrating the multi-anode PMTs, a two-dimensional projection image of the square scintillator telescope hit by cosmic muons is demonstrated. By performing a cosmic test with the Micromegas telescope, the position resolution of the detector was determined to reach approximately 8.6 mm, which is close to the value obtained in physical simulation.

Keywords Plastic scintillator · Multi-anode PMT · WLS fiber · Position resolution

This work was supported by the Strategic Priority Research Program on Space Science of Chinese Academy of Sciences (No. XDA04070900).

✉ Yun-Long Zhang
ylzhang@ustc.edu.cn

1 State Key Laboratory of Particle Detection and Electronics, University of Science and Technology of China, Hefei 230026, China

2 Department of Modern Physics, University of Science and Technology of China, Hefei 230026, China

3 Department of Physics, University of Science and Technology of China, Hefei 230026, China

1 Introduction

Plastic scintillators are commonly used in high-energy physics owing to their excellent optical transmission properties, simple production, low cost, and high performance in particle detections [1–3]. They have often served as an anticoincidence detector to provide a trigger signal [4–6]. However, scintillators are seldom used in position measurement owing to their poor position resolution [7]. Accordingly, a position-sensitive plastic scintillator detector is developed to realize position measurement and provide trigger information simultaneously.

A position-sensitive detector can be used for various applications. For example, combined with muon tomography, which is a technique that uses cosmic ray muons to generate three-dimensional images of volumes, the detector can be applied in the field of security imaging [8, 9]. In the USA, the Decision Sciences International Corporation (DSIC) has implemented muon tracker technology in a multi-mode passive detection system (MMPDS) [10]. This port scanner located in Freeport, Bahamas, can detect shield nuclear material, explosive, and contraband. A study of the image characterization metrics for MMPDS shows that the spatial resolution is centimeter magnitude order [10]. Therefore, a position-sensitive plastic scintillator may be applied in the field of homeland security owing to its large area and low cost. The spatial resolution must be of centimeter magnitude order.

In this paper, the design of grooves on the top and bottom sides of a plastic scintillator in which wavelength-shifting (WLS) fibers can be embedded is proposed. Alternate WLS fibers are gathered and routed to a multi-anode photomultiplier (PMT) for each dimension [11]. The scintillator detector is thus considered to be segmented into several small tiles in two dimensions. The design method was tested using physical simulation and an experiment.

This paper is organized as follows. In Sect. 2, we describe the design of the detector, including the plastic scintillator, grooves, and WLS fibers. In Sect. 3, we present a Monte Carlo simulation based on GEANT4 to estimate the position resolution. Section 4 describes the fabrication of the detector in detail. In Sect. 5, details of the calibration of multi-anode PMT are provided, and the results of cosmic test are presented.

2 Detector design

The size of the plastic scintillator used in this design is $320 \times 320 \times 25\ \mathrm{mm}^3$, with 16 grooves milled uniformly on each side. Each groove is 9.5 mm in width and 1.1 mm in depth, as shown in Fig. 1. They are approximately 19.32 mm apart from each other, and nine WLS fibers of diameter 1 mm are embedded within each of them. Sixteen of these WLS bundles in the x-dimension correspond, respectively, to the 16 channels of the multi-anode PMT. Therefore, the plastic scintillator is considered to be divided into 16 tiles in the x-dimension. Furthermore, the 16 WLS-fiber bundles in the y-dimension are arranged in the same way as in the x-dimension and they correspond to the y-dimension of the multi-anode PMT. Therefore, the plastic scintillator is considered to be segmented into 16×16 tiles in two dimensions [12].

The outputs of the multi-anode PMTs are connected to the front-end electronics (FEE) board and the data acquisition (DAQ) system, with which the hitting position of an incident particle can be reconstructed in two dimensions.

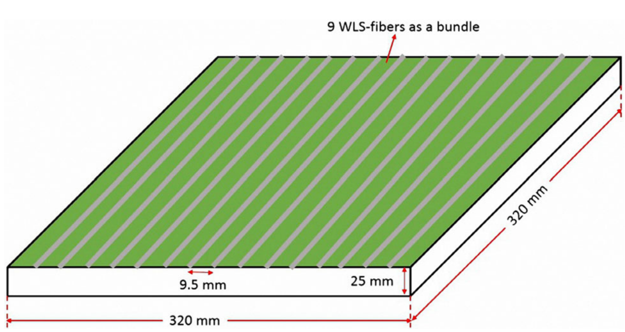

Fig. 1 (Color online) Structure schematic of the plastic scintillator in the x-dimension. Each groove is 9.5 mm in width and 1.1 mm in depth, and nine WLS fibers are embedded in each groove

3 Physical simulation

To understand the scintillator detector with WLS-fiber readout more intuitively, a model of the detector was built using GEANT4, which is the most commonly used simulation software in high-energy physics [13, 14]. The scintillator detector was constructed according to the design method described above.

Consider a muon of 2 GeV passing through the detector. Its energy is deposited and converted into fluorescence in the detector. Subsequently, fluorescent photons are transmitted in the scintillator and absorbed by the WLS-fiber bundles. The distribution of fluorescence transport is shown in Fig. 2.

We subsequently counted the quantities of fluorescent photons absorbed by each fiber bundle and reconstructed the center of distribution of fluorescence, which is defined as the hitting position of the muon event, by using the barycenter method. The reconstructed position is not fixed but obeys a Gaussian distribution, owing to system error and other factors. In this study, the sigma value fitting with Gaussian distribution is regarded as the position resolution. As shown in Fig. 3, the position resolution of the detector with WLS-fiber readout reaches approximately 5 mm in the Monte Carlo simulation, which indicates the feasibility of the design.

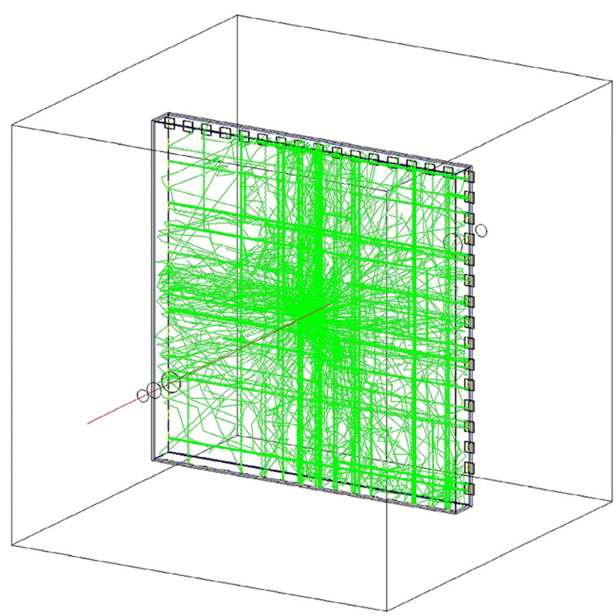

Fig. 2 (Color online) Fluorescence transmission in the detector. The green lines represent the fluorescence activated by the muons hitting the center of the scintillator detector

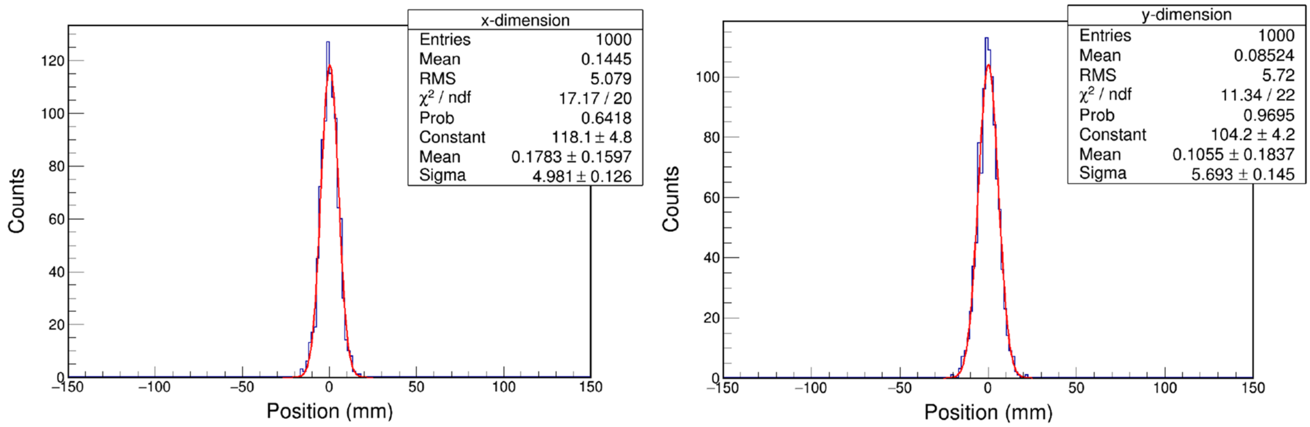

Fig. 3 Position of the incident muons hitting the center of the detector is indicated by the horizontal axis, and the count of florescent photons is indicated by the vertical axis. The sigma value of the fitting Gaussian waveform can be regarded as the position resolution. The left graph shows the reconstructed position resolution in the x-dimension, and the right graph shows the reconstructed position resolution in the y-dimension

4 Detector fabrication

A piece of BC414 produced by Saint-Gobain with the dimensions of $320 \times 320 \times 25$ mm^3 was milled using a programmable milling machine according to the design method described above. After the completion of milling, the scintillator was annealed at 70 °C for 3 h to remove any remaining stress in order to avoid crazing and consequent performance degradation [15].

To optimize light collection [16, 17], the BCF-92 was used to match the absorption spectrum of WLS fibers to the emitting spectrum of the plastic scintillator. The BCF-92 [18], also produced by Saint-Gobain, is a kind of WLS and light-transmitting fiber, with an emission peak at 492 nm. The EJ-500 [19], produced by Eljen Technology, is a clear and colorless epoxy cement and is ideal for optically bonding plastic scintillators and fibers. The H8711 (manufactured by Hamamatsu) was used to match the emission wavelength of the BCF-92. Its quantum efficiency is approximately 30% at 490 nm [20]. Moreover, the H8711 has 4×4 anodes correspondingly reading out the fluorescent signals of the 16 WLS bundles. An adapter guides the 16 WLS bundles to the corresponding 16 cathode cells of the multi-anode PMT in the x-dimension. Another adapter performs the same task in the y-dimension. By placing this arrangement into a large black box of size $440 \times 440 \times 50$ mm^3 to protect the scintillator detector from external light, the preparation was completed. The fabrication process was as follows:

1. Cut the WLS fibers to the appropriate length and polish the end surfaces.
2. Assemble nine WLS fibers as one bundle (16 bundles in all).
3. Fix all the WLS bundles into an adapter and ensure that their ends are all located in a plane; these are the readout ends of the fibers.
4. Place the WLS bundles into the corresponding grooves of the scintillator, and the other end of the fibers is covered with the reflective material.
5. Glue the WLS bundles with EJ-500 and wait for them to dry (approximately 24 h).
6. Combine the multi-anode PMT with the WLS bundles, and thus, the fabrication of the x-dimension of the detector is complete.
7. Construct the y-dimension of the detector by repeating the above steps.

A photograph of the position-sensitive scintillator detector is shown in Fig. 4.

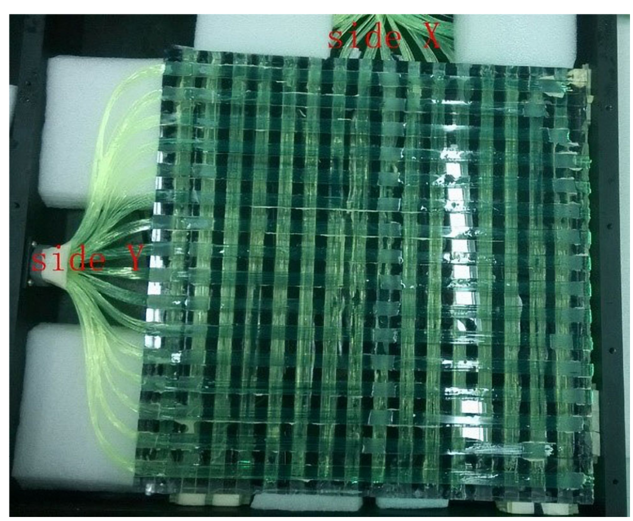

Fig. 4 (Color online) Prototype of the position-sensitive scintillator detector

With an appropriate multi-anode PMT base design, the 16 channels of charge signals from each multi-anode PMT can be coupled to the FEE board consisting of a VA32 ASIC [21], which has 32 analog input channels for measuring the charge signals. Each channel is composed of a charge-sensitive preamplifier (CSA), CR-RC-shaping amplifier, and sample–hold circuit. Therefore, the PMT output charge signals are integrated by the CSA and thereafter shaped into a semi-Gaussian pulse with a peaking time of approximately 1.8 μs. Furthermore, a hold signal is used to sample all the analog channels.

Subsequently, the output current signals obtained from the VA32 chip are wired together and led to a current-to-voltage conversion circuit, digitized using a 16-bit analog-to-digital converter (ADC, AD976A [22]). When a trigger is provided by PMT dynode signals or the telescope system, the ADC digital output data are recorded by the DAQ system [23].

5 Calibration and cosmic test

5.1 Calibration of multi-anode PMTs

As two multi-anode PMTs are used in the design, their gain should be calibrated first. The peak of a single photoelectron can be used as the calibration parameter because of its linearity to the gain. Figure 5 shows a block diagram of the LED calibration system.

The LED lights are driven by the pulse generator, whose output voltage can be adjusted to vary the light intensity. The photoelectron peak becomes the main part of the spectrum for each anode channel of the calibrating PMT, as shown in Fig. 6. A random trigger is used to obtain the pedestal in the test.

After the calibration, 16 spectra of each multi-anode PMT in the x- (and y-) dimensions were obtained. By choosing one of the ADC peak channels as a gain reference, the others can be normalized. The relative ratios are

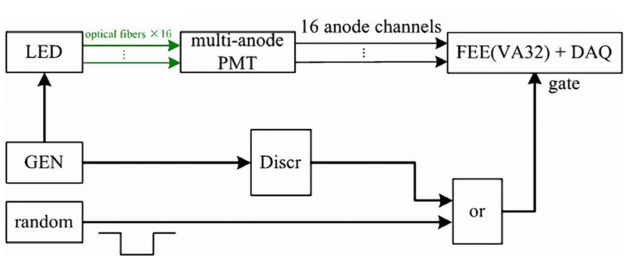

Fig. 5 Block diagram of the multi-anode PMT calibration system. The pulse generator drives the LED glitter, and the LED lights can be collected by 16 entrance windows of the multi-anode PMT using 16 optical fibers. The LED light intensity can also be varied by adjusting the output voltage of the pulse generator

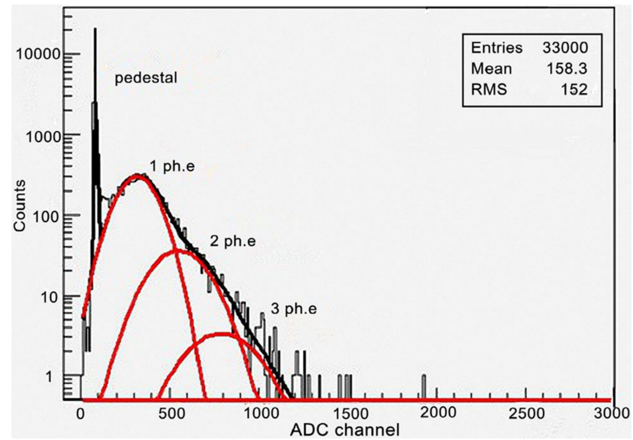

Fig. 6 (Color online) Typical fitting of the photoelectron spectrum of a channel of the multi-anode PMT. The ADC count of the signal is indicated by the horizontal axis, and the event count is indicated by the vertical axis. The peaks of pedestal, single photoelectron, and double photoelectron are fitted

demonstrated in Fig. 7, and they can be used as the normalization factors for the ADC counts of the corresponding anodes in position reconstruction.

In addition, the cross talk of the multi-anode PMT is less than 1%, as presented in the datasheet [20]. Therefore, it is believed that the effect of cross talk for different anodes can be ignored in the experiment.

5.2 Cosmic test

A telescope system is required to study the performance of the detector with WLS-fiber readout [24]. First, two small plastic scintillator detectors (20×20 mm^2) were used as the telescope system—one each placed above and below the detector, as shown in Fig. 8.

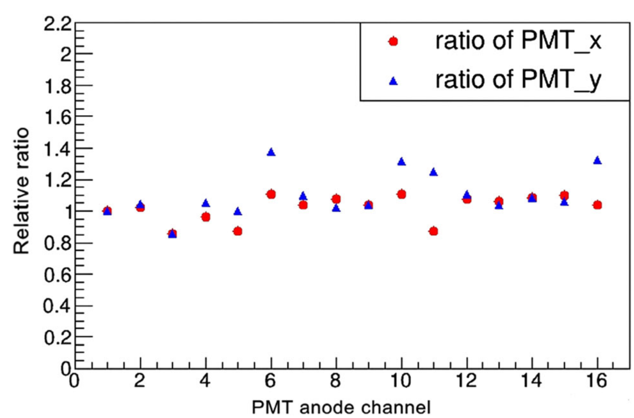

Fig. 7 (Color online) After the calibration of the multi-anode PMT, the relative ratios of the anodes are indicated by the vertical axis, and their channel numbers are indicated by the horizontal axis. The red points represent the ratios of multi-anode PMT in the x-dimension, and the blue triangles represent the ratios of multi-anode PMT in the y-dimension

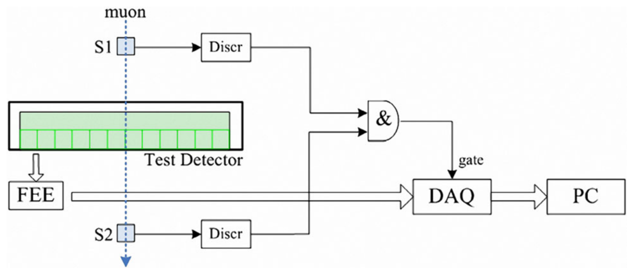

Fig. 8 Block diagram of the cosmic test with two small plastic scintillator detectors. The two detectors, S1 and S2, are placed above and below the test detector, respectively, and used as the telescope system

Cosmic muon events were triggered by the small scintillator telescope. When the logic (S1 * S2) equaled one, the data of the ADC counts from each of the 16 readout channels of the x- and y- dimensions were collected. First, the response efficiency of the detector was obtained by adjusting the voltage of the multi-anode PMTs. By comparing the event counts passing through the telescope and the event counts passing through the test detector, the detection efficiencies of the test detector under different voltages can be calculated. As shown in Fig. 9, the detection efficiency is over 90% when the voltage exceeds 790 V. The working voltage of the PMT in the following test is set to 800 V.

Thus, the position where the cosmic muons pass through the test detector can be reconstructed using the barycenter method. Consider the x-dimension. When a triggered incident muon (ith event) passes through the test detector, its position can be reconstructed using the following formula:

$$\text{position}_i = \frac{\sum_{j=1}^{16} w_j\left(x_j - x_\text{o}\right) \times 19.32}{\sum_{j=1}^{16} w_j},$$

where $w_j = \frac{\text{ADC\_count}_j - \text{ped}_j}{\text{ratio}_j}$ indicates the corrected position weight of the jth channel; ADC_count$_j$ indicates the ADC count of the jth channel; ped$_j$ represents the pedestal of the jth channel; ratio$_j$ indicates the relative gain ratio of the jth channel; and x_j indicates the jth anode channel of the PMT in x-dimension. The center of the detector ($x_\text{o} = 8.5, y_\text{o} = 8.5$) is defined as the zero point.

Figure 10 shows the scatter points of reconstructed cosmic events passing through the telescope and test detector. The distribution of scatter points is only a projection image of the telescope hit by cosmic muons.

To evaluate the position resolution of the detector, it is necessary to consider another telescope with better spatial resolution. In this case, Micromegas (MM) detectors with submillimeter position resolution [25] were used as the telescope system. During the cosmic test, two MM detectors were placed above and below the detector, as shown in Fig. 8, with MMI and MM2 replacing S1 and S2, respectively. Both the DAQ of the test detector and the MM telescope were synchronized by the trigger (MM1*MM2). Hence, the track of an incident muon (ith event) can be identified using the two Micromegas detectors. It is regarded as the reference track (i) and is across the test detector at (x_{ir}, y_{ir}) for the ith event. Moreover, the hitting position (x_{it}, y_{it}) of the ith muon passing through the test detector can be reconstructed using the ADC data from the x- and y-dimensions of the multi-anode PMTs. The

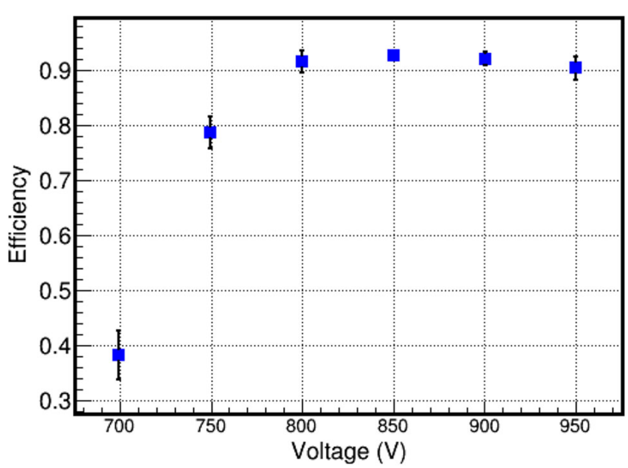

Fig. 9 Plateau curve of the detection efficiency. When the voltage exceeds 800 V, the efficiency tends to be steady. A slight drop of the efficiency after the voltage exceeds 850 V may be due to the excessive voltage, and the maximum voltage of the multi-anode PMT is ~ 1000 V

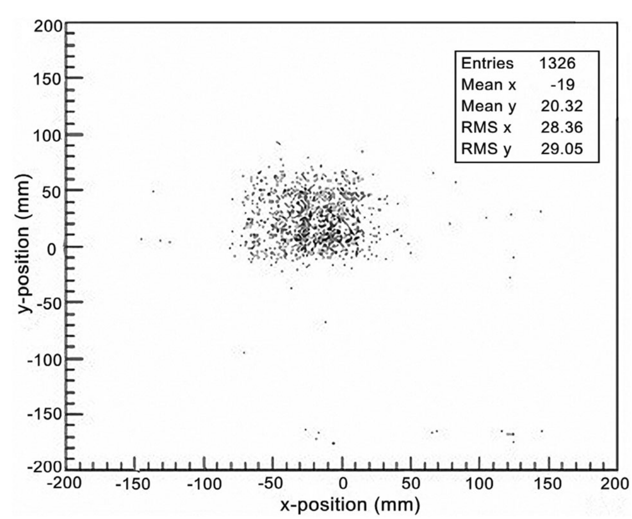

Fig. 10 Two-dimensional projection image of detector obtained using the small telescope, and the data accumulated for ten hours. The hitting position of the incident muons in the x-dimension is indicated by the horizontal axis, and the position in the y-dimension is indicated by the vertical axis

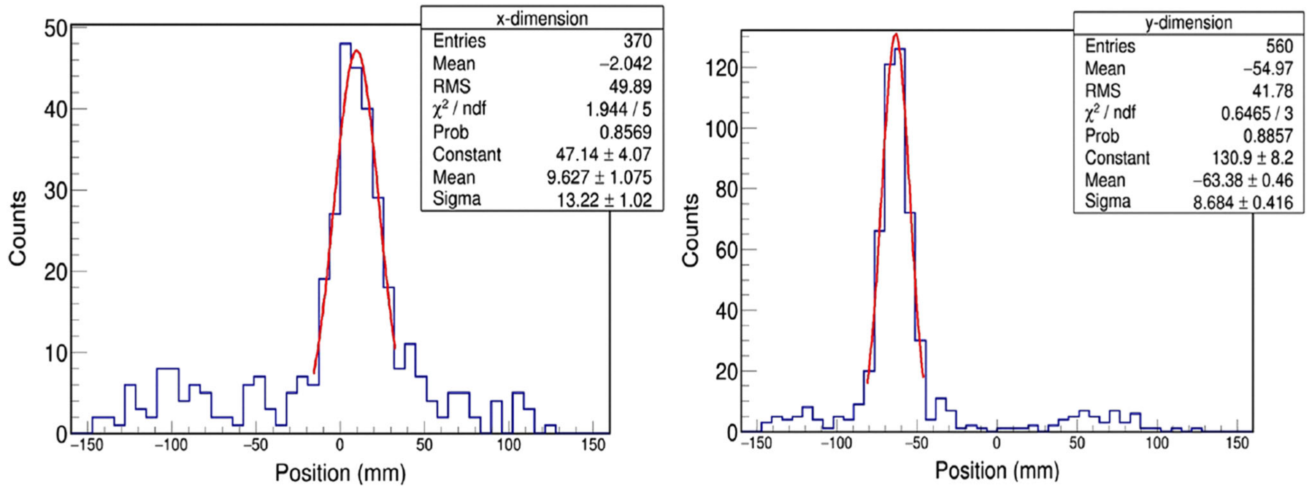

Fig. 11 Residuals of the test position and the reference position are indicated by the horizontal axis, and the event count is indicated by the vertical axis. Thus, the sigma of the fitting Gaussian waveform can be considered as the position resolution. The left graph shows the position resolution in the x-dimension, and the right graph shows the position resolution in the y-dimension

residuals are defined as $\Delta x_i \equiv x_{it} - x_{ir}$ and $\Delta y_i \equiv y_{it} - y_{ir}$ and are calculated event by event.

Figure 11 shows the histograms of Δx (left) and Δy (right). The fitted position resolution of the detector is approximately 8.6 mm.

6 Conclusion

In this paper, the design and fabrication of a position-sensitive plastic scintillator detector with WLS-fiber readout were presented. The performance of the detector was also studied. The results of the cosmic test showed that the positions of the incident particles can be reconstructed in two dimensions with a detector and the position resolution can be as high as approximately 8.6 mm, which is close to the simulation result (approximately 5 mm).

Acknowledgements The authors are grateful to Chi Wang, Ji-Jie Lou, and all the teachers and students who have helped the authors during this study. The cosmic tests described in this paper were conducted at the University of Science and Technology of China.

References

1. J.B. Birks, *The Theory and Practice of Scintillation Counting* (Pergamon Press, New York, 1964)
2. A. Pla-Dalmau, A.D. Bross, K.L. Mellott, Low-cost extruded plastic scintillator. Nucl. Instrum. Methods A **466**, 482–491 (2001). https://doi.org/10.1016/S0168-9002(01)00177-2
3. N. Zaitseva, B.L. Rupert, I. PaweLczak et al., Plastic scintillators with efficient neutron/gamma pulse shape discrimination. Nucl. Instrum. Methods A **668**, 88–93 (2012). https://doi.org/10.1016/j.nima.2011.11.071
4. A.A. Moiseevo, R.C. Hartman, J.F. Ormes et al., The anti-coincidence detector for the GLAST large area telescope. Astrophysics **27**, 339–358 (2007). https://doi.org/10.1016/j.astropartphys.2006.12.003
5. F. Perotti, M. Fiorini, S. Incorvaia et al., The AGILE anticoincidence detector. Nucl. Instrum. Methods A **556**, 228–236 (2006). https://doi.org/10.1016/j.nima.2005.10.016
6. G. Tabacaru, A. Azhari, J. Brinkley et al., Scattering of ^{7}Be and ^{8}B and the astrophysical S_{17} factor. Phy. Rev. C **73**, 025808 (2006). https://doi.org/10.1103/PhysRevC.73.025808
7. S.A. Pozzi, J.A. Mullens, J.T. Mihalczo, Analysis of neutron and photon detection position for the calibration of plastic (BC-420) and liquid (BC-501) scintillators. Nucl. Instrum. Methods A **524**, 92–101 (2004). https://doi.org/10.1016/j.nima.2003.12.036
8. J.S. Larry, M.F. Andrew, L.M. Christopher, Statistical reconstruction for cosmic ray muon tomography. IEEE Trans. Image Process. (2007). https://doi.org/10.1109/tip.2007.901239
9. S. Riggi, P. La Rocca, E. Leonora et al., GEANT4 simulation of plastic scintillator strips with embedded optical fibers for a prototype of tomographic system. Nucl. Instrum. Methods A **624**, 583–590 (2010). https://doi.org/10.1016/j.nima.2010.10.012
10. W. Luo, A. Lehovich, E. Anashkin et al., Image characterization metrics for muon tomography, in *Proceedings of the SPIE 9073, Chemical, Biological, Radiological, Nuclear, and Explosives (CBRNE) Sensing,* XV, vol. 907317 (2014). https://doi.org/10.1117/12.2049972
11. T. Matsumoto, S. Korpar, I. Adachi et al., Studies of proximity focusing RICH with an aerogel radiator using flat-panel multi-anode PMTs (Hamamatsu H8500). Nucl. Instrum. Methods A **521**, 367–377 (2004). https://doi.org/10.1016/j.nima.2003.11.384
12. S. Kurosawa, H. Kubo, K. Hattori et al., Performance of 8 × 8 pixel LaBr 3: Ce and Gd2SiO5: Ce scintillator arrays coupled to a 64-channel multi-anode PMT. IEEE T Nucl. Sci. (2009). https://doi.org/10.1109/tns.2009.2034657
13. S. Agostinelli, J. Allison, K. Amako et al., GEANT4-a simulation toolkit. Nucl. Instrum. Methods A **506**, 250–303 (2003). https://doi.org/10.1016/S0168-9002(03)01368-8
14. S. Riggi, R. La Rocca, E. Leonora et al., GEANT4 simulation of plastic scintillator strips with embedded optical fibers for a prototype of tomographic system. Nucl. Instrum. Methods A **624**, 583–590 (2010). https://doi.org/10.1016/j.nima.2010.10.012
15. A.A. Moiseev, P.L. Deering, R.C. Hartman et al., High efficiency plastic scintillator detector with wavelength-shifting fiber readout

for the GLAST large area telescope. Nucl. Instrum. Methods A **583**, 372–381 (2007). https://doi.org/10.1016/j.nima.2007.09.040
16. L. Archambault, J. Arsenault, L. Gingras et al., Plastic scintillation dosimetry: optimal selection of scintillating fibers and scintillators. Med. Phys. **32**, 2271–2278 (2005). https://doi.org/10.1118/1.1943807
17. G. Suft, G. Anton, R. Bogendorfer et al., A scintillating fibre detector for the crystal barrel experiment at ELSA. Nucl. Instrum. Methods A **538**, 416–424 (2005). https://doi.org/10.1016/j.nima.2004.09.029
18. *Saint-Gobain Crystals, Scintillating Fiber BCF-92*. http://www.crystals.saint-gobain.com/uploadedFiles/SG-Crystals/Documents/SGC%20Fibers%20Brochure.pdf
19. Eljen Technology, *OPTICAL CEMENT EJ-500*. http://www.eljentechnology.com/images/products/data_sheets/EJ-500.pdf
20. Hamamatsu, *16ch Multi Anode PMT Assembly h8711 Datasheet.* https://www.hamamatsu.com/resources/pdf/etd/H8711_TPMH1320E.pdf
21. IDEAS, 33 *Channel High-Dynamic Range CSA with Sample-and-Hold*. http://www.ideas.no/products/va32hdr14-3/
22. ANALOG DEVICES, 16-Bit, 100kSPS/200kSPS BiCMOS A/D Converters. http://www.analog.com/media/en/technical-documentation/data-sheets/AD976_976A.pdf
23. C. Feng, D. Zhang, J. Zhang et al., Design of the readout electronics for the BGO calorimeter of DAMPE mission. IEEE T. Nucl. Sci. (2015). https://doi.org/10.1109/tns.2015.2479091
24. R. Huber, J. Lang, S. Navert et al., Search for time-reversal violation in the β decay of polarized ^{8}Li nuclei. Phys. Rev. Lett. **90**, 202301 (2003). https://doi.org/10.1103/PhysRevLett.90.202301
25. Z. Zhang, F. Wang, Z. Yang et al., Manufacture and performance of the thermal-bonding micromegas prototype. J. Instrum. **9**, C10028 (2014). https://doi.org/10.1088/1748-0221/9/10/C10028